

Research Article

Sensing Fractional Power Spectrum of Nonstationary Signals with Coprime Filter Banks

Xiaomin Li,^{1,2} Huali Wang ,³ Wanghan Lv,⁴ and Haichao Luo⁵

¹School of Electronic and Optical Engineering, Nanjing University of Science and Technology, Nanjing, China

²School of Mechanical and Electrical Engineering, Henan Institute of Science and Technology, Xinxiang, China

³College of Communication, The Army Engineering University of PLA, Nanjing, China

⁴Research Institute of China Electronics Technology Group Corporation, Nanjing, China

⁵College of Tourism, Henan Normal University, Xinxiang, Henan 453003, China

Correspondence should be addressed to Huali Wang; huali.wang@ieee.org

Received 29 February 2020; Revised 17 June 2020; Accepted 29 June 2020; Published 17 July 2020

Academic Editor: Yan-Ling Wei

Copyright © 2020 Xiaomin Li et al. This is an open access article distributed under the Creative Commons Attribution License, which permits unrestricted use, distribution, and reproduction in any medium, provided the original work is properly cited.

The coprime discrete Fourier transform (DFT) filter banks provide an effective scheme of spectral sensing for wide-sense stationary (WSS) signals in case that the sampling rate is far lower than the Nyquist sampling rate. And the resolution of the coprime DFT filter banks in the Fourier domain (FD) is $|2\pi/(MN)|$, where M and N are coprime. In this work, a digital fractional Fourier transform- (DFrFT-) based coprime filter banks spectrum sensing method is suggested. Our proposed method has the same sampling principle as the coprime DFT filter banks but has some advantages compared to the coprime DFT filter banks. Firstly, the fractional power spectrum of the chirp-stationary signals which are nonstationary in the FD can be sensed effectively by the coprime DFrFT filter banks because of the linear time-invariant (LTI) property of the proposed system in discrete-time Fourier domain (DTFD), while the coprime DFT filter banks can only sense the power spectrum of the WSS signals. Secondly, the coprime DFrFT filter banks improve the resolution from $|2\pi/(MN)|$ to $|2\pi \sin \alpha/(MN)|$ by combining the fractional filter banks theory with the coprime theory. Simulation results confirm the obtained analytical results.

1. Introduction

Power spectrum plays an important role in signal processing such as array processing [1–4], spectral estimation [5–7], signal detection and estimation [8–12], and so on. As the traditional methods of sensing power spectrum are associated with wide-sense stationary (WSS) signals whose second-order expectations remain unchanged over time, the conventional methods are under Fourier analysis [13–19], and all these developments have led to satisfactory results.

Compared with the WSS signals, the nonstationary signals are characterized by being oriented along an oblique axis in the time-frequency domain while the stationary signals are projected in a horizontal direction. And as a spot treatment in the frequency domain, the conventional Fourier analysis does not allow associating events in the time

domain with the frequency domain, so Fourier analysis is not a useful tool for processing nonstationary signals.

As a generalized form of the Fourier transform (FT), the fractional Fourier transform (FrFT) [20, 21] allows the signals in the time-frequency domain to be projected onto a line of arbitrary angle. In contrast to the standard Fourier analysis, the fractional Fourier analysis has a notable potential in the treatment of nonstationary signals due to an additional degree of freedom. The analysis of nonstationary signals by means of the fractional Fourier transformation has been reported [22–24]. And many signal processing theories in the Fourier domain (FD) have been extended to the fractional Fourier domain (FrFD) based on the relationship between FrFT and FT, such as the filters theory [25–29], the correlation theory [30–32], and the power spectral density theory [33, 34].

Meanwhile, it is necessary to sense a wide band of power spectrum, leading to prohibitively high Nyquist rates which will exceed the specifications of best commercial analog-to-digital converters (ADCs). Therefore, designing a sub-Nyquist sampling scheme which can effectively sense the power spectrum of nonstationary signals is a challenging task. Coprime theory [35, 36], which is well suited for analyzing sparsely sampled signals in case that sampling rate is far lower than the Nyquist sampling rate, has gained increasing attention in recent years. Coprime theory can be well coupled with DFT filter banks theory in temporal domain to sense the power spectrum of WSS signals [35]. In [35], the WSS premise of the input signals ensures the decimate operation in cross-correlation that can be coupled with coprimality well (see (13)); therefore, when the inputs are nonstationary, i.e., the second-order expectations of the input sequence change over time [37–40], the decimate operation cannot be performed to introduce the coprime theory in, resulting in inefficient sensing of the power spectrum for nonstationary signals. Thus, the coprime DFT filter banks [35] is not suitable to process nonstationary signals.

Recently, several research efforts based on the coprime DFT filter banks [35] are developed from different aspects. Huang et al. [41] applied two simple operations on each low-rate data channel of the original coprime DFT filter banks to form a 0.5 frequency resolution shifted analyzer and synthesized it and the original coprime DFT filter banks to remove all the annoying spurious peaks. However, many decision thresholds were needed to set in the modified analyzer, so the modified analyzer is not suitable for engineering applications. In an attempt to completely remove the spurious-peak side effect, Xiangdong Huang and Yuxuan [42] proposed a high-performance coprime spectral analysis method based on paralleled all-phase point-pass filtering; the proposed method can not only completely remove the spurious-peak side effect, but also can be implemented easily in the real-world application. Vaidyanathan and Pal [43] extended one-dimensional coprime DFT filter banks to multiple dimensions. Wu and Liang [44] used short-time Fourier transform to segment the nonstationary signals into piecewise stationary signals. However, the window function in short-time Fourier transform has the trade-off between temporal resolution and frequency resolution, resulting in low estimation accuracy for the power spectrum.

This paper aims to develop a coprime digital fractional Fourier transform (DFrFT) filter banks theory for sensing the fractional power spectrum of the chirp stationary signals, which are nonstationary in the usual sense or in the FD [22, 33]. We describe how to construct a sub-Nyquist system by using two low-speed coprime sampling ADCs and two DFrFT filter banks and derive the mathematical expression of the output, which shows that the proposed system can effectively sense the fractional power spectrum of nonstationary signals without loss of any information.

First, following the coprime premise and the property of the low-pass filter in discrete-time fractional Fourier domain (DTFrFD), we construct the coprime pair of DFrFT filter banks and prove the uniqueness of its passband in

corresponding DTFD (with its argument scaled by $\csc \alpha$) (see Section 3.3 for details). Second, we prove that the coprime pair of DFrFT filter banks is linear time invariant (LTI) in DTFD based on the low-pass filter theory in DTFrFD, as the corresponding chirp modulated forms of the nonstationary signals are stationary, the decimate operation can be performed in the cross-correlation analysis between the outputs of the coprime pair of DFrFT filter banks, and the conventional power spectrum of the stationary signals can be acquired based on the uniqueness of the passband (see section 3.4 for details). Third, in terms of the polyphase representation of the filters in DTSFrFD, the decimator at the output of the filters can be moved to the left of the polyphase subfilters, resulting in an efficient coprime DFrFT filter banks (see Section 3.5 for details). Further, based on the fractional power spectrum theory, the final fractional power spectrum of the nonstationary signals can be acquired by the proposed coprime DFrFT filter banks. Besides, when the input is deterministic signal, the cross-correlations give the sensing of the spectrum in DTFrFD based on the fractional convolution theory (see Section 4.1 for details). The modified architecture not only senses the nonstationary signals but also has an accurate resolution $|\frac{2\pi \sin \alpha}{MN}|$ in DTFD.

The outline of this paper is as follows. In Section 2, the problem formulation is introduced based on the basic preliminaries. In Section 3, the coprime DFrFT filter banks for sensing the fractional power spectrum of nonstationary signals is elaborated. In Section 4, the special cases for deterministic signals are discussed, and the performance of the proposed method is analyzed in terms of the resolution and the fractional spectrum estimation.

2. Preliminaries

2.1. DTSFrFT. The FrFT is a generalization of the FT, which essentially allows the signals in the time-frequency domain to be projected onto a line of arbitrary angle [21, 22]. Simplified fractional Fourier transform (SFrFT) [45] has the same effect as FrFT of order α for filter design, but for digital implementation, it is simpler than the original FrFT. In digital signal processing systems, the signals used are digital signals sampled from the analog signals; their representations in simplified fractional Fourier domain (SFrFD) should be obtained by discrete-time simplified fractional Fourier transform (DTSFrFT). The DTSFrFT of $x(n)$ is defined as follows [45]:

$$\bar{X}_\alpha(\omega) = A_\alpha \sum_{n=-\infty}^{\infty} x(nT) e^{j1/2(nT)^2 \cot \alpha - j\omega n c s c \alpha}, \quad (1)$$

where $\omega = uT$ is the digital frequency of u , which is the variable in SFrFD, and T is the sample spacing in temporal domain.

And we have

$$\bar{X}_\alpha(\omega) = e^{-j\omega^2/2T^2 \cot \alpha} \tilde{X}_\alpha(\omega), \quad (2)$$

where $\bar{X}_\alpha(\omega)$ is the DTSFrFT of $x(n)$ and $\tilde{X}_\alpha(\omega)$ is the DTFrFT of $x(n)$.

2.2. *The Low-Pass Filter in DTSFrFD.* Suppose $h(n)$, $n = 0, 1, \dots, N-1$ is a low-pass filter with length N , and its frequency response is $\tilde{H}(\tilde{\omega})$, i.e.,

$$\tilde{H}(\tilde{\omega}) = \begin{cases} 1, & |\tilde{\omega}| < \tilde{\omega}_c, \\ 0, & \text{otherwise,} \end{cases} \quad (3)$$

where $\tilde{\omega}$ is the digital frequency in discrete-time Fourier domain (DTFD) and $\tilde{\omega}_c$ is the cutoff frequency. Let $h_0(n) = h(n)e^{-j1/2n^2(\Delta t)^2 \cot \alpha}$, and its fractional frequency response is $\bar{H}_\alpha(\omega)$, $\bar{H}_\alpha(\omega) = A_\alpha \sum_{n=-\infty}^{\infty} h_0(n)e^{j1/2n^2(\Delta t)^2 \cot \alpha - j\omega n \csc \alpha} = A_\alpha \tilde{H}(\omega \csc \alpha)$ [26], i.e.,

$$\bar{H}_\alpha(\omega) = A_\alpha \tilde{H}(\tilde{\omega} \csc \alpha), \quad (4)$$

where ω is the digital frequency in DTSFrFD and $\tilde{H}(\tilde{\omega} \csc \alpha)$ is the frequency response of $h(n)$ with its argument scaled by $\csc \alpha$. $\bar{H}_\alpha(\omega)$ is defined as the fractional frequency response of low-pass filter in DTSFrFD. Equation (4) shows that $\bar{H}_\alpha(\omega)$, the low-pass filter in DTSFrFD, is equivalent to the discrete-time Fourier transform (DTFT) of $h(n)$, $n = 0, 1, \dots, N-1$ with its argument scaled by $\csc \alpha$. So, $\bar{H}_\alpha(\omega)$ is linear time invariant (LTI) in DTFD. And this relation is the instrument for the signal polyphase representation and filter bank theorems in DTSFrFD as will be discussed later.

2.3. The α^{th} Chirp-Stationary Signal

Definition 1 (the α^{th} chirp-stationary signal). For a non-stationary random signal $x(t)$, if the chirp modulated form $\tilde{x}(t) = x(t)\exp(j(t^2/2)\cot \alpha)$ of $x(t)$ is stationary, i.e., $R_{\tilde{x}\tilde{x}}(t_1, t_2) = R_{\tilde{x}\tilde{x}}(\tau)|_{\tau=t_1-t_2}$, where $R_{\tilde{x}\tilde{x}}(\bullet)$ is the autocorrelation of $\tilde{x}(t)$, the signal $x(t)$ is called the α^{th} chirp-stationary signal.

And we have an important result for $x(t)$.

Theorem 1 (see [34]). *The relationship between the α^{th} fractional power spectrum of $x(t)$ and the conventional power spectrum of $\tilde{x}(t)$ is*

$$\tilde{P}_x(u \csc \alpha) = \sqrt{\frac{1}{1 + j \cot \alpha}} P_{xx}^\alpha(u), \quad (5)$$

where $\tilde{P}_x(u \csc \alpha)$ is the conventional power spectrum of stationary signal $\tilde{x}(t)$ and $P_{xx}^\alpha(u)$ is the α^{th} fractional power spectrum of nonstationary signal $x(t)$.

2.4. *Convolution Theorem in DTSFrFD.* For any discrete-time sequences $x(nT)$ and $h(nT)$, the discrete-time fractional Fourier convolution is as follows [32]:

$$y(nT) = x(nT) \overset{\alpha}{*} h(nT) = A_\alpha e^{-j1/2n^2 T^2 \cot \alpha} \left(x(nT) e^{j1/2n^2 T^2 \cot \alpha} * h(nT) e^{j1/2n^2 T^2 \cot \alpha} \right), \quad (6)$$

where $\overset{\alpha}{*}$ denotes the fractional convolution operator. $*$ denotes the traditional convolution operator. T is the sample spacing in temporal domain. The discrete-time fractional

Fourier transform (DTFrFT) of $y(nT)$ can be denoted as follows:

$$\tilde{Y}_\alpha(\omega) = e^{-j\omega^2/2T^2 \cot \alpha} \tilde{X}_\alpha(\omega) \tilde{H}_\alpha(\omega), \quad (7)$$

where $\tilde{Y}_\alpha(\omega)$, $\tilde{X}_\alpha(\omega)$, and $\tilde{H}_\alpha(\omega)$ are the DTFrFT of $y(nT)$, $x(nT)$, and $h(nT)$. And the DTSFrFT of $y(nT)$ can be denoted as follows:

$$\bar{Y}_\alpha(\omega) = \bar{X}_\alpha(\omega) \bar{H}_\alpha(\omega), \quad (8)$$

where $\bar{Y}_\alpha(\omega)$, $\bar{X}_\alpha(\omega)$, and $\bar{H}_\alpha(\omega)$ are the DTSFrFT of $y(nT)$, $x(nT)$, and $h(nT)$. Combining equations (6) and (8) illustrates that the discrete-time fractional Fourier convolution of $x(nT)$ and $h(nT)$ is corresponding to the product of $\bar{X}_\alpha(\omega)$ and $\bar{H}_\alpha(\omega)$ in DTSFrFD. Similarly, suppose $y(nT) = e^{-j1/2n^2 T^2 \cot \alpha} (x(nT) e^{j1/2n^2 T^2 \cot \alpha} * h(nT))$.

Then,

$$\tilde{Y}_\alpha(\omega) = \sqrt{2\pi} \tilde{X}_\alpha(\omega) \tilde{H}_\alpha(\omega), \quad (9)$$

where $\tilde{Y}_\alpha(\omega)$, $\tilde{X}_\alpha(\omega)$ are the DTFrFT of $y(nT)$, $x(nT)$ and $\tilde{H}_\alpha(\omega)$ is the DTSFrFT of $h(nT)$.

2.5. *Original Coprime DFT Filter Banks.* The coprime pair of DFT filter banks introduced in [35] which is illustrated in Figure 1 has a unique passband with the width $\Delta\tilde{\omega}$ and the center $i\Delta\tilde{\omega}$ in the Fourier domain (FD) (see [35] for details). As a result, any stimulus component near $i\Delta\tilde{\omega}$, $i \in Z^+$, can be uniquely identified by the product filter banks.

In Figure 1, the cross-correlation between $u_k(n)$ and $v_l(n)$ is

$$E[u_k(n)v_l^*(n)] = \int_0^{2\pi} S_{xx}(e^{j\tilde{\omega}}) G_l^*(e^{j\tilde{\omega}}) H_k(e^{j\tilde{\omega}}) \frac{d\tilde{\omega}}{2\pi}, \quad (10)$$

where $S_{xx}(e^{j\tilde{\omega}})$ is the power spectrum of $x(n)$ which is the common WSS input of the two filter banks and $G_l(e^{j\tilde{\omega}})$ and $H_k(e^{j\tilde{\omega}})$ are the frequency response of filters $G_l(z)$ and $H_k(z)$, respectively, which are acquired through applying zooming and shifting operations on the transfer curve of ideal lowpass filters $H(z)$ (or $G(z)$) using the shift parameter k (or l). In terms of the properties of the unique passband in the FD, equation (10) can be approximately written as

$$E[u_k(n)v_l^*(n)] \approx c S_{xx}(e^{j\tilde{\omega}_i}), \quad (11)$$

where c is a constant which depends on the exact passband shapes and on the coprime pair M and N and $\tilde{\omega}_i = 2\pi i/MN$. Further, based on the wide-sense stationary (WSS) premise of input $x(n)$, time domain averages can be used to estimate correlations:

$$\frac{1}{L} \sum_{n=0}^{L-1} E[u_k(n)v_l^*(n)] \approx c S_{xx}(e^{j\tilde{\omega}_i}), \quad (12)$$

and since $u_k(n)$ and $v_l(n)$ are outputs of LTI systems with a common WSS input $x(n)$, they are jointly WSS, so

$$\frac{1}{L} \sum_{n=0}^{L-1} E[u_k(nMN)v_l^*(nMN)] \approx c S_{xx}(e^{j\tilde{\omega}_i}), \quad (13)$$

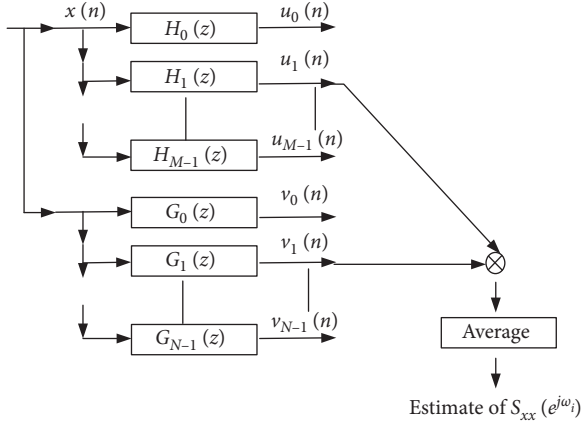


FIGURE 1: A coprime pair of DFT filter banks. Here, M and N are coprime.

where M and N are coprime. That is, we can simply multiply decimated versions of $u_k(n)$ and $v_l(n)$ and perform the averaging. Then, based on the polyphase forms of filters $H_k(z)$ and $G_l(z)$, the decimator $\downarrow MN$ can be combined with $H_k(z)$ and $G_l(z)$ to realize the coprime decimate for input signal $x(n)$ as shown in Figure 2. Besides, in Figure 2, $x_u(n)$ and $x_v(n)$ can be, respectively, acquired by employing two analog-to-digital converters (ADCs) with the sampling rates $f_{s1} = 1/MT$, $f_{s2} = 1/NT$ to discretize a continuous signal $x(t)$.

3. The Proposed Architecture

3.1. Problem Formulation. From the above description in Section 2.5, the coprime DFT filter banks architecture [35] as shown in Figure 2 which can sense the power spectrum of stationary signals effectively is constructed based on two points: the passband uniqueness and WSS premise. The passband uniqueness ensures that any stimulus component near the passband can be uniquely identified by the product filter banks, i.e., the equivalence relationship in equation (11). And the WSS premise guarantees the decimated operation in equation (13) which can be combined with the polyphase representation of the filters to achieve the coprime sampling structure as shown in Figure 2. Accordingly, when the input signal $x(n)$ is not WSS, the decimated operation cannot be performed so that the coprime theory cannot be coupled with DFT filtering bank theory to derive the architecture in Figure 2.

3.2. System Description. In this paper, we introduce the fractional Fourier analysis theory (the fractional filters theory and the fractional power spectrum theory) into the original coprime DFT filter banks to derive a modified architecture for sensing the fractional power spectrum of the chirp-stationary signals. First, we construct the coprime pair of DFrFT filter banks which is shown in Figure 3 and prove the uniqueness of their passband in DTFD (see Section 3.3 for details). Second, we implement the cross-correlation between the outputs of the two filter banks; then based on the properties of the low-pass filter in DTSFrFD introduced

in Section 2.2 and the uniqueness of the passband, the cross-correlation analysis can be converted from DTFrFD into DTFD. As the coprime pair of DSFrFT filter banks is LTI in corresponding DTFD (see Section 3.4 for details) and the input signal is stationary when it is modulated by a corresponding chirp signal, the decimated operation can be performed successfully. Third, in terms of the polyphase representation of the filters in DTSFrFD (see Section 3.5 for details), the decimator at the output of the filters can be moved to the left of the polyphase subfilters, resulting in an efficient polyphase implementation. Further, based on Theorem 4 (see Section 3.6 for details), the final fractional power spectrum of the nonstationary signals can be acquired. And the proposed coprime filter banks is shown in Figure 4.

3.3. The Coprime Pair of DFrFT Filter Banks and the Uniqueness of Their Passband. We specifically take advantage of the coprimality of M and N to construct a coprime pair of DFrFT filter banks by combining an M band DFrFT filter bank and an N band DFrFT filter bank. And the proposal is illustrated in Figure 3. In this system, the two filter banks are composed of M and N subfilters $\bar{H}_{k,\alpha_2}(\omega)$, $k = 0, \dots, M-1$, $\bar{G}_{l,\alpha_2}(\omega)$, $l = 0, \dots, N-1$, respectively, which can be acquired through applying zooming and shifting operations on the transfer curve of the ideal low-pass filter $\bar{H}_{\alpha_2}(\omega)$, $\bar{G}_{\alpha_2}(\omega)$ in DTSFrFD. And we will prove in the following that the product filter $\bar{F}_{lk,\alpha_2}(\omega)$ has a unique passband with the width $\Delta\omega$ and the center $i\Delta\omega$.

Assume that $\bar{H}_{\alpha_2}(\omega) = A_{\alpha_2} \tilde{H}(\omega \csc \alpha_2)$ is the ideal low-pass filter in DTSFrFD.

$$\bar{H}_{\alpha_2}(\omega) = \begin{cases} A_{\alpha_2}, & |\tilde{\omega}| \leq \frac{\pi \sin \alpha_2}{M}, \\ 0, & \text{otherwise.} \end{cases} \quad (14)$$

And $\omega = uT$ is the digital frequency in DTSFrFD; $\tilde{\omega}$ is the digital frequency in DTFD. Thus, $\bar{H}_{\alpha_2}(N\omega)$ has N passbands in DTFD, with each passband having width $2\pi \sin \alpha_2 / MN$. $\bar{H}_{k,\alpha_2}(\omega) = \bar{H}_{\alpha_2}(e^{j\tilde{\omega}N \csc \alpha_2} U_M^k)$, $k = 0, \dots, M-1$, where $U_M \triangleq e^{-j2\pi \sin \alpha_2 / M}$, can be rewritten as

$$\begin{aligned} \bar{H}_{k,\alpha_2}(\omega) &= \bar{H}_{\alpha_2}\left(e^{j\tilde{\omega}N \csc \alpha_2} U_M^k\right) \\ &= \bar{H}_{\alpha_2}\left(e^{j(\tilde{\omega} \csc \alpha_2 - 2\pi k \sin \alpha_2 / MN)N}\right), \quad (15) \\ &k = 0, \dots, M-1. \end{aligned}$$

These are shifted version of $\bar{H}_{\alpha_2}(N\omega)$, in increments of $2\pi \sin \alpha_2 / (MN)$, for each k in $0 \leq k \leq M-1$, $\bar{H}_{k,\alpha_2}(\omega)$ has N passbands, each passband has width $2\pi \sin \alpha_2 / (MN)$, and the N passbands are centered at $2\pi n \sin \alpha_2 / N + 2\pi k \sin \alpha_2 / MN = (Mn + k)2\pi \sin \alpha_2 / MN$, $0 \leq n \leq N-1$.

Similarly, assume that $\bar{G}_{\alpha_2}(\omega) = A_{\alpha_2} \tilde{G}(\tilde{\omega} \csc \alpha_2)$ is the ideal low-pass filter in DTSFrFD.

$$\bar{G}_{\alpha_2}(\omega) = \begin{cases} A_{\alpha_2}, & |\tilde{\omega}| \leq \frac{\pi \sin \alpha_2}{N}, \\ 0, & \text{otherwise.} \end{cases} \quad (16)$$

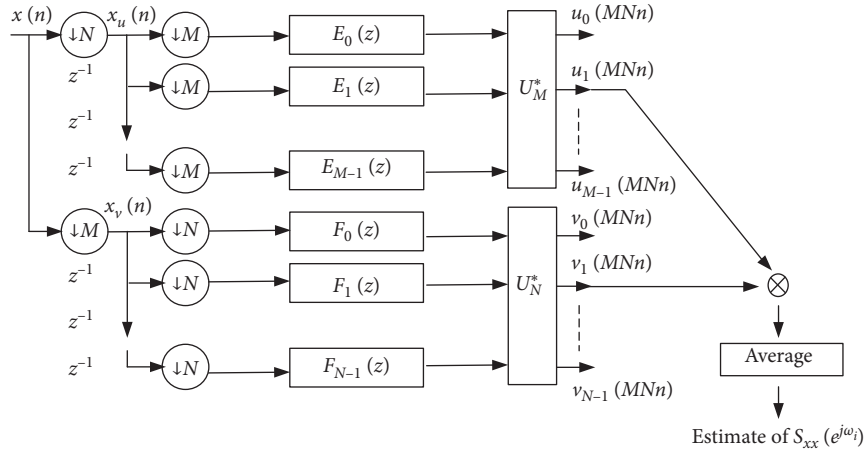


FIGURE 2: Coprime DFT filter banks.

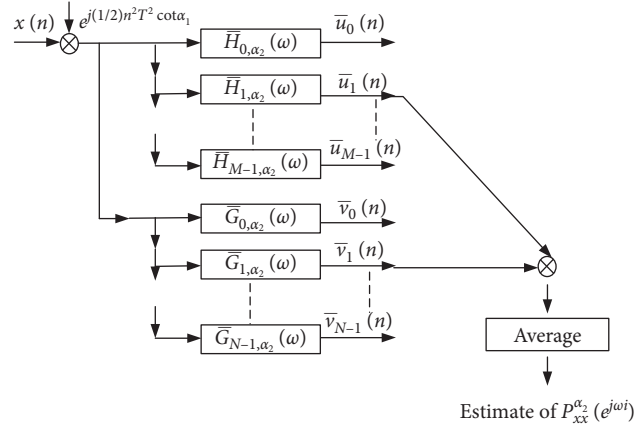


FIGURE 3: The coprime pair of DFrFT filter banks.

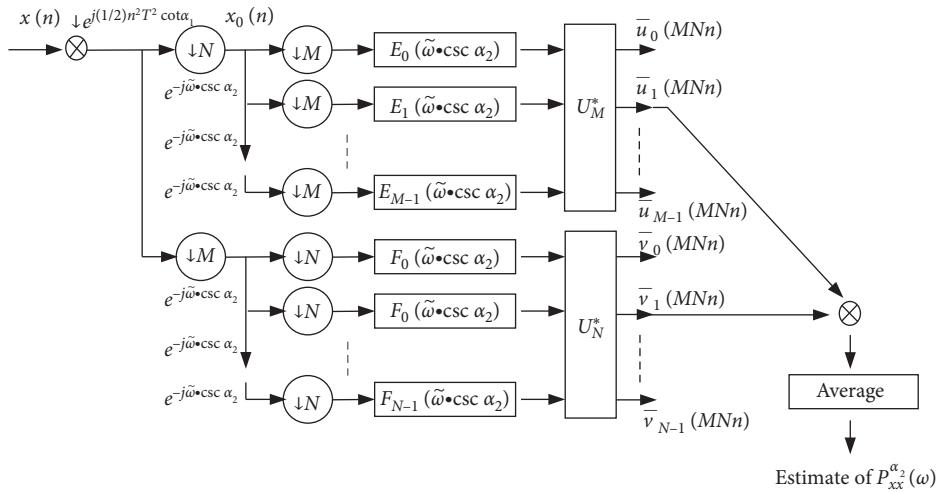


FIGURE 4: The polyphase representation of the coprime pair of DFrFT filter banks.

Thus, $\bar{G}_{\alpha_2}(M\omega)$ has M passbands in DTFD, with each passband having width $2\pi \sin \alpha_2 / (MN)$. $\bar{G}_{l,\alpha_2}(\omega) = \bar{G}_{\alpha_2}(e^{j\tilde{\omega}M \text{csc } \alpha_2} U_N^l)$, $l = 0, \dots, N-1$, where $U_N \triangleq e^{-j2\pi \sin \alpha_2 / N}$, can be rewritten as

$$\begin{aligned} \bar{G}_{l,\alpha_2}(\omega) &= \bar{G}_{\alpha_2}\left(e^{j\tilde{\omega}M \text{csc } \alpha_2} U_N^l\right) \\ &= \bar{G}_{\alpha_2}\left(e^{j\tilde{\omega} \text{csc } \alpha_2 - 2\pi \sin \alpha_2 / MN} M\right), \end{aligned} \quad (17)$$

$$l = 0, \dots, N-1,$$

these are shifted version of $\bar{G}_{\alpha_2}(M\omega)$, in increments of $2\pi \sin \alpha_2/(MN)$, for each l in $0 \leq l \leq N-1$, $\bar{G}_{l,\alpha_2}(\omega)$ has M passbands, each passband has width $2\pi \sin \alpha_2/(MN)$, and the M passbands are centered at $2\pi m \sin \alpha_2/M + 2\pi l \sin \alpha_2/MN = (Nm + l)2\pi \sin \alpha_2/MN$, $0 \leq m \leq M-1$.

For the two filter banks $\bar{H}_{k,\alpha_2}(\omega)$, $k = 0, \dots, M-1$, $\bar{G}_{l,\alpha_2}(\omega)$, $l = 0, \dots, N-1$, now consider the product of the k^{th} and l^{th} responses $\bar{H}_{k,\alpha_2}(\omega)$ and $\bar{G}_{l,\alpha_2}(\omega)$:

$$\begin{aligned} \bar{F}_{kl,\alpha_2}(\omega) &= \bar{H}_{k,\alpha_2}(\omega)\bar{G}_{l,\alpha_2}(\omega) \\ &= \bar{H}_{\alpha_2}\left(e^{j\omega N \csc \alpha_2} \mathbf{U}_M^k\right) \bar{G}_{\alpha_2}\left(e^{j\omega M \csc \alpha_2} \mathbf{U}_N^l\right), \end{aligned} \quad (18)$$

and there are two important theorems as follows:

Theorem 2. *Given any integer i in $0 \leq l \leq MN-1$, there is a unique $\bar{F}_{kl,\alpha}(\omega)$, i.e., a unique (k,l) pair, with passband centered at $2\pi i \sin \alpha/(MN)$.*

Theorem 3. *$\bar{F}_{kl,\alpha}(\omega)$ has precisely one passband, and it has width $2\pi \sin \alpha/(MN)$. That is, there is only one overlapping band among the N bands of $\bar{H}_{k,\alpha}(\omega)$ and M bands of $\bar{G}_{l,\alpha}(\omega)$. This overlapping passband is centered at $2\pi i \sin \alpha/(MN)$ for some integer i in $0 \leq l \leq MN-1$. The proofs are in Appendix A and Appendix B.*

Figure 5 demonstrates how the filters work for $M = 4$ and $N = 3$. As shown in Figure 5, the filter $\bar{H}_{\alpha_2}(N\omega)$ has three passbands, and each has width $2\pi \sin \alpha_2/12$. There are four distinct shifted versions of $\bar{H}_{\alpha_2}(N\omega)$, $\bar{H}_{k,\alpha_2}(\omega) = \bar{H}_{\alpha_2}(e^{j\omega N \csc \alpha_2} \mathbf{U}_4^k)$, $0 \leq k \leq 3$. The filter $\bar{G}_{\alpha_2}(M\omega)$ has four passbands, and each has width $2\pi \sin \alpha_2/12$. There are three distinct shifted versions of $\bar{G}_{\alpha_2}(M\omega)$, $\bar{G}_{l,\alpha_2}(\omega) = \bar{G}_{\alpha_2}(e^{j\omega M \csc \alpha_2} \mathbf{U}_3^l)$, $0 \leq l \leq 2$. Each shifted version $\bar{G}_{l,\alpha_2}(\omega)$ overlaps with any shifted version $\bar{H}_{k,\alpha_2}(\omega)$ in precisely one passband. Therefore, the product $\bar{F}_{kl,\alpha_2}(\omega)$ is bandpass with a single passband, having width $2\pi \sin \alpha_2/12$. Furthermore, the twelve combinations of (k,l) produce twelve distinct filters $\bar{F}_{kl,\alpha_2}(\omega)$, covering $0 \leq \omega < 2\pi \sin \alpha_2$. Therefore, we get the effect of an MN -band filter bank in DTFD by combining one M -band filter bank with one N -band filter bank.

3.4. The Cross-Correlation Analysis. In this part, we will analyze the cross-correlation between the outputs of the two filter banks $\bar{H}_{k,\alpha_2}(\omega)$ and $\bar{G}_{l,\alpha_2}(\omega)$ in Figure 3 to acquire their corresponding decimated versions, which will be combined with the polyphase representation of DSFrFT filters in Section 3.5 to form the structure in Figure 4.

Assume the two filter banks $\bar{H}_{k,\alpha_2}(\omega)$ and $\bar{G}_{l,\alpha_2}(\omega)$ in Figure 3 have a common α_1^{th} chirp-stationary random sequence $x(n)$ as the input, with sample spacing T ; let $\tilde{x}(n) = x(n)e^{jn^2T^2/2 \cot \alpha_1}$; as known in Definition 2 in Section 3.6, $\tilde{x}(n)$ is the traditional WSS sequence with autocorrelation $\bar{R}_{xx}(a)$, $\bar{R}_{xx}(a) = E[\tilde{x}(k)\tilde{x}(k+a)]$. The two filter banks $\bar{H}_{k,\alpha_2}(\omega)$, $k = 0, \dots, M-1$, and $\bar{G}_{l,\alpha_2}(\omega)$, $l = 0, \dots, N-1$, have M , N outputs, respectively. Now take the k^{th} output $\bar{u}_k(n)$ of the filter bank $\bar{H}_{k,\alpha_2}(\omega)$ and the l^{th} output $\bar{v}_l(n)$ of the filter bank $\bar{G}_{l,\alpha_2}(\omega)$. The cross-correlation between $\bar{u}_k(n)$ and $\bar{v}_l(n)$ is

$$\begin{aligned} &E[\bar{u}_k(n)\bar{v}_l^*(n)] \\ &= E[(\tilde{x}(n) * h_k(n))(\tilde{x}^*(n) * g_l^*(n))] \\ &= E\left[\sum_{i_1} \sum_{i_2} \tilde{x}(i_1)\tilde{x}^*(i_2)h_k(n-i_1)g_l^*(n-i_2)\right] \\ &= \sum_{i_1} \sum_{i_2} E[\tilde{x}(i_1)\tilde{x}^*(i_2)]h_k(n-i_1)g_l^*(n-i_2). \end{aligned} \quad (19)$$

Letting $a = i_1 - i_2$, we have $E[\bar{u}_k(n)\bar{v}_l^*(n)] = \sum_{i_1} \sum_{i_2} \bar{R}_{xx}(a)h_k(n-i_1)g_l^*(n-i_2) = \sum_a \bar{R}_{xx}(a)g_{kl}^*(a)$, where $\bar{R}_{xx}(a)$ is the autocorrelation of $\tilde{x}(n)$, $g_{kl}(a) = \sum_n h_k(n)g_l^*(n+a)$. Since $\bar{G}_{l,\alpha_2}(\tilde{\omega} \csc \alpha_2) = \bar{H}_{k,\alpha_2}(\tilde{\omega} \csc \alpha_2) \bar{G}_{l,\alpha_2}^*(\tilde{\omega} \csc \alpha_2)$,

Parseval's relation yields

$$\begin{aligned} &E[\bar{u}_k(n)\bar{v}_l^*(n)] \\ &= \frac{1}{2\pi} \int_0^{2\pi} \bar{P}_x(\tilde{\omega} \csc \alpha_2) \bar{H}_{k,\alpha_2}(\tilde{\omega} \csc \alpha_2) \cdot \bar{G}_{l,\alpha_2}^*(\tilde{\omega} \csc \alpha_2) d\tilde{\omega}, \end{aligned} \quad (20)$$

where $\bar{P}_x(\tilde{\omega} \csc \alpha_2)$ is the power spectrum of $\tilde{x}(n)$. Since M and N are coprime, the product filter $\bar{H}_{k,\alpha_2}(\tilde{\omega} \csc \alpha_2) \bar{G}_{l,\alpha_2}(\tilde{\omega} \csc \alpha_2)$ has a single passband, with width $2\pi \sin \alpha_2/MN$, and center at $2\pi i \sin \alpha_2/MN$, for some integer i in $0 \leq l \leq MN-1$. For large MN , the product $\bar{H}_{k,\alpha_2}(\tilde{\omega} \csc \alpha_2) \bar{G}_{l,\alpha_2}(\tilde{\omega} \csc \alpha_2)$ is a very narrow band filter, and so

$$E[\bar{u}_k(n)\bar{v}_l^*(n)] \approx A\bar{P}_x(\tilde{\omega} \csc \alpha_2), \quad (21)$$

and A is a constant which depends on the exact passband shapes, M and N . Assuming the WSS process of $\tilde{x}(n)$ is ergodic, we use time domain averages to estimate correlations:

$$\frac{1}{L} \sum_{n=0}^{L-1} [\bar{u}_k(n)\bar{v}_l^*(n)] \approx A\bar{P}_x(\tilde{\omega} \csc \alpha_2), \quad (22)$$

where L refers to the number of consumed snapshots. As can be seen from Section 2.2, for the low-pass filter $\bar{H}_{\alpha_2}(\omega)$ in DTSFrFD, there is $\bar{H}_{\alpha_2}(\omega) = A_{\alpha_2} \bar{H}(\tilde{\omega} \csc \alpha_2)$, where $\bar{H}(\tilde{\omega} \csc \alpha_2)$ is the DTFT of $h(n)$. Thus, $\bar{H}_{\alpha_2}(\omega)$, the low-pass filter in DTSFrFD, is equivalent to $\bar{H}(\tilde{\omega} \csc \alpha_2)$, which is the low-pass filter in DTFD. Accordingly, $\bar{H}_{\alpha_2}(\omega)$ is LTI in DTFD. And filter banks $\bar{H}_{k,\alpha_2}(\omega)$ and $\bar{G}_{l,\alpha_2}(\omega)$ are LTI in DTFD. Therefore, $\bar{u}_k(n)$ and $\bar{v}_l(n)$ are outputs of LTI systems with a common WSS input $\tilde{x}(n)$; they are jointly WSS, so

$$\frac{1}{L} \sum_{n=0}^{L-1} [\bar{u}_k(nK)\bar{v}_l^*(nK)] \approx A\bar{P}_x(\tilde{\omega} \csc \alpha_2), \quad (23)$$

for any integer K . That is, we can simply multiply decimated versions of $\bar{u}_k(n)$ and $\bar{v}_l(n)$ and perform the averaging.

3.5. The Polyphase Representation of DSFrFT Filters. Suppose $\bar{E}_q(M\tilde{\omega} \csc \alpha_2)$ is the q^{th} -type I polyphase component of $h(n)$ which has been defined in Section 2.2, i.e.,

$$\bar{H}(\tilde{\omega} \csc \alpha_2) = \sum_{q=0}^{M-1} e^{-jq\tilde{\omega} \csc \alpha_2} \bar{E}_q(M\tilde{\omega} \csc \alpha_2), \quad (24)$$

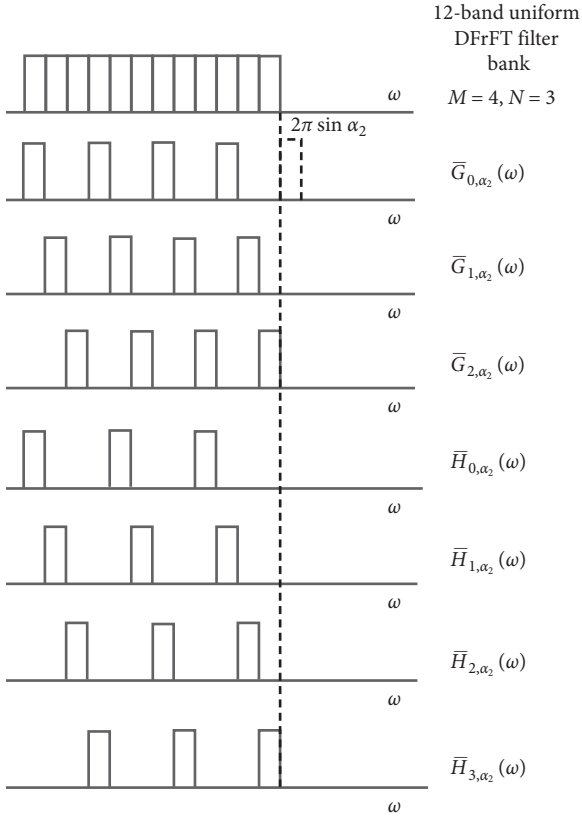


FIGURE 5: The filters $\bar{H}_{\alpha_2}(N\omega)$ and $\bar{G}_{\alpha_2}(M\omega)$, and their shifted versions, demonstrated for $M = 4$ and $N = 3$.

where $\tilde{E}_q(M\tilde{\omega} \text{csc} \alpha_2) = \sum_{n=0}^{+\infty} h_0(Mn+q)e^{-j(M\tilde{\omega})n \text{csc} \alpha_2}$.
Substituting (24) into (4),

$$\bar{H}_{0, \alpha_2}(\omega) = A_{\alpha_2} \sum_{q=0}^{M-1} e^{-jq\tilde{\omega} \text{csc} \alpha_2} \tilde{E}_q(M\tilde{\omega} \text{csc} \alpha_2). \quad (25)$$

Equation (25) is the equivalence polyphase representation of $\bar{H}_{\alpha_2}(\omega)$ in DTFD. In most applications, the decimator is preceded by a low-pass digital filter called the decimation filter. And according to equation (25), the equivalent polyphase implementation of low-pass decimation filter in DTFD is illustrated in Figure 6.

Accordingly, since

$$\bar{H}_{\alpha_2}\left(\omega - \frac{2\pi k \sin \alpha_2}{M}\right) \quad (26)$$

$$= A_{\alpha_2} \sum_{q=0}^{M-1} e^{-jNq\tilde{\omega} \text{csc} \alpha_2} U_M^{-kq} \tilde{E}_q(MN\tilde{\omega} \text{csc} \alpha_2),$$

$$\bar{H}_{\alpha_2}\left(N\left(\omega - \frac{2\pi k \sin \alpha_2}{MN}\right)\right) \quad (27)$$

$$= A_{\alpha_2} \sum_{q=0}^{M-1} e^{-jNq\tilde{\omega} \text{csc} \alpha_2} U_M^{-kq} \tilde{E}_q(MN\tilde{\omega} \text{csc} \alpha_2),$$

$$0 \leq k \leq M-1.$$

So, we can represent the filters $\bar{H}_{0, \alpha_2}(\omega)$ in appropriate polyphase forms:

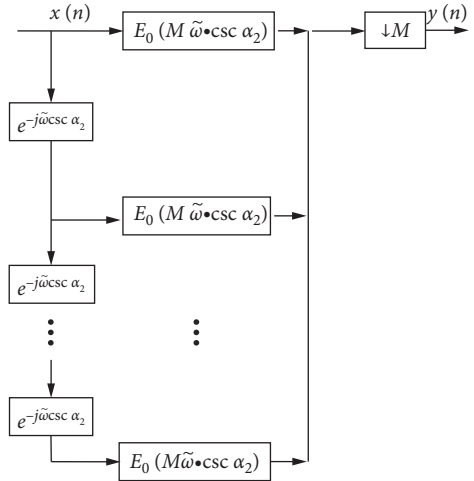


FIGURE 6: The equivalent polyphase implementation of low-pass decimation filter in DTFD.

$$\bar{H}_{0, \alpha_2}(\omega) = A_{\alpha_2} \sum_{q=0}^{M-1} e^{-jNq\tilde{\omega} \text{csc} \alpha_2} U_M^{-kq} \tilde{E}_q(MN\tilde{\omega} \text{csc} \alpha_2), \quad (28)$$

$$0 \leq k \leq M-1.$$

Figure 7 shows the polyphase forms of the filters $\bar{H}_{0, \alpha_2}(\omega)$ in DTFD. Similarly, the polyphase forms of the filters $\bar{G}_{l, \alpha_2}(\omega)$ are

$$\bar{G}_{l, \alpha_2}(\omega) = A_{\alpha_2} \sum_{q=0}^{M-1} e^{-jMq\tilde{\omega} \text{csc} \alpha_2} U_M^{-lq} \tilde{F}_q(MN\tilde{\omega} \text{csc} \alpha_2), \quad (29)$$

$$0 \leq l \leq N-1,$$

and its polyphase forms in DTFD are shown in Figure 8. And we have the noble identities of decimator [46] which is shown in Figure 9. Such interconnections arise when we try to use the polyphase representation for decimation filters. And we can redraw Figure 6 as Figure 10. Accordingly, combining with the analysis in Section 3.4, when decimation ratio $K = MN$, an efficient polyphase implementation coprime DSFrFT filter banks under coprime sampling is shown in Figure 4. Besides, in Figure 4, $x_0(n)$ and $x_1(n)$ can be, respectively, acquired by employing two ADCs with the sampling rates $f_{s1} = 1/MT$, $f_{s2} = 1/NT$ to discretize a continuous signal $x(t)e^{j1/2t^2 \cot \alpha_1}$.

3.6. The Fractional Power Spectrum of Nonstationary Signals in DTSFrFD. In this section, we will prove that the output of the architecture in Figure 4 is the fractional power spectrum of nonstationary signals $x(n)$. To make it more clear, we first define the chirp stationarity random sequence.

Definition 2 (the α^{th} chirp-stationary random sequence). For nonstationary random sequence $x(n)$, if $\tilde{x}(n) = x(n)e^{jn^2T^2/2 \cot \alpha}$ is a stationary random sequence, we call $x(n)$ the α^{th} chirp-stationary random sequence.

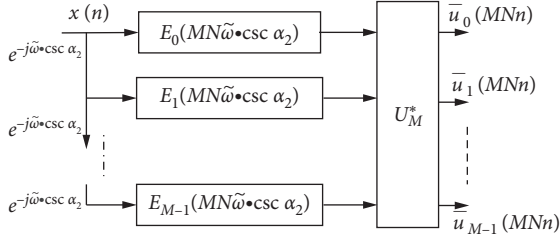


FIGURE 7: The polyphase representation of $\bar{H}_{0,\alpha_2}(\omega)$.

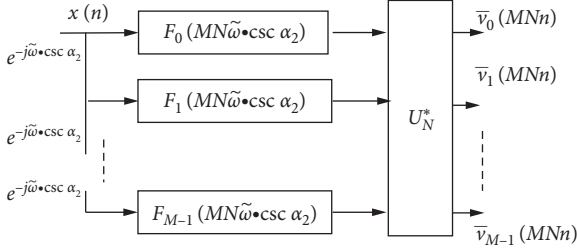


FIGURE 8: The polyphase representation of $\bar{G}_{l,\alpha_2}(\omega)$.

And a useful conclusion associated with the fractional power spectrum of $x(n)$ is shown here for convenience.

Theorem 4. *The relationship between the α^{th} fractional power spectrum of the α^{th} chirp-stationary random sequence $x(n)$ and the conventional power spectrum of the stationary random sequence $\tilde{x}(n)$ is*

$$\bar{P}_x(\tilde{\omega} \text{csc } \alpha) = \sqrt{\frac{1}{1 + j \cot \alpha}} P_{xx}^\alpha(\omega), \quad (30)$$

in which $\bar{P}_x(\tilde{\omega} \text{csc } \alpha)$ is the conventional power spectrum of $\tilde{x}(n)$ in DTFD and $P_{xx}^\alpha(\omega)$ is the α^{th} fractional power spectrum of $x(n)$ in DTSFrFD. See Appendix C for the certification process.

Therefore, as can be seen from equation (30), except for a constant coefficient, $\bar{P}_x(\tilde{\omega} \text{csc } \alpha)$ has the same spectral shape with $P_{xx}^\alpha(\omega)$. So, a traditional spectral estimate of the chirp-stationary sequence $\tilde{x}(n)$ is transformed into the simplified fractional spectral estimation of the nonstationary sequence $x(n)$. So, equation (23) can be rewritten as

$$\frac{1}{L} \sum_{n=0}^{L-1} [u_k(nK)v_l(nK)] \approx A \sqrt{\frac{1}{1 + j \cot \alpha}} P_{xx}^{\alpha_2}(\omega), \quad (31)$$

where A is a constant which depends on the exact passband shapes, M and N . That is, in DTSFrFD, the output of the system as shown in Figure 4 is the α_2^{th} fractional power spectrum of $x(n)$ multiplied by a constant.

3.7. Choice of the Transform Orders α_1 and α_2 . As shown in Figure 4, there are two transform orders α_1 and α_2 to be determined. The transform order α_1 is used to convert nonstationary signals into stationary signals, while α_2 decides the resolution of the proposed system which partially influences the sensing accuracy.

The received α_1^{th} chirp-stationary signal is composed of a modulated signal and noise. Its model is given by

$$x(n) = s(n) + \eta(n), \quad (32)$$

where $x(n)$ and $s(n)$ are received signal and modulated signal, respectively. $\eta(n)$ is assumed to be additive white Gaussian noise.

The modulated signal $s(n)$ is given by $s(n) = A \exp(-j(2\pi f_c n / f_{NYQ} + \phi(n) + \phi_0))$, where A is the amplitude, and f_c and ϕ_0 are the carrier frequency and the initial uniformly distributed random phase, respectively. f_{NYQ} is the Nyquist sampling rate. $\phi(n)$ is the phase function, which determines the modulation type of the signal. For simplicity and without loss of generality, we assume that A is an invariant constant.

In Definition 1, we know that for the α_1^{th} chirp-stationary signal $x(t)$, its chirp modulated form $\tilde{x}(t) = x(t) \exp(j(t^2/2) \cot \alpha_1)$ is stationary, i.e., $R_{\tilde{x}\tilde{x}}(t_1, t_2) = R_{\tilde{x}\tilde{x}}(\tau)|_{\tau=t_1-t_2}$; therefore, the transform order $\alpha_1 = \arccot(-\partial\phi(n)/\partial n)$.

In the fractional Fourier domain (FrFD), support of signals' change is associated with the transform order, and there exists an optimum transform order in which the energy of signals is maximally concentrated [30–32]. When a signal is transformed by FrFT at its optimum order, transform kernel acts as a matched filter. Therefore, the transform order α_2 is equal to the optimal transform which can maximize the absolute amplitude, i.e., $\alpha_2 = \alpha_{\text{opt}}$.

Furthermore, since the energy of Gaussian noise signals cannot effectively concentrate in FrFD, the Gaussian noise can be suppressed effectively.

The optimal transformation order α_{opt} corresponding to maximum magnitude obtained from the FrFT is given by $\alpha_{\text{opt}} = \max[|F_\alpha(t, u)|^2]$,

where $F_\alpha(t, u)$ is the FrFT of the stationary signal $\tilde{x}(t) = x(t) \exp(j(t^2/2) \cot \alpha_1)$ in the α -order FrFD. And α_{opt} will directly affect the sensing performance; hence, the method of searching the optimal order is important. The traditional method to get the optimal order in the DTSFrFD is peak sweeping method [32, 33], which is an easy method to realize. And obviously, the search-based algorithms require numerous extra calculations and have the contradiction between estimation performance and complexity.

In this section, we introduce the normalized second-order central moment (NSOCM) calculation method [47] to directly obtain the optimal transformation order α_{opt} in DTSFrFD. Compared with the search-based algorithms, the NSOCM approach has higher computational efficiency because of its nonergodic search mechanism.

According to [47], the optimal order α_{opt} is normally given by

$$\alpha_{\text{opt}} = \arg \min_{\alpha} \text{TBP}\{X_\alpha(u)\}, \quad 0 \leq \alpha < \pi, \quad (33)$$

where $\text{TBP}\{X_\alpha(u)\}$ is the time-bandwidth product for $X_\alpha(u)$, and the NSOCM p_α of $X_\alpha(u)$ is defined by

$$p_\alpha = \int_{-\infty}^{\infty} (u - m_\alpha)^2 |X_\alpha(u)|^2 du / \int_{-\infty}^{\infty} |X_\alpha(u)|^2 du = \omega_\alpha - m_\alpha^2, \quad (34)$$



FIGURE 9: The noble identities of decimators.

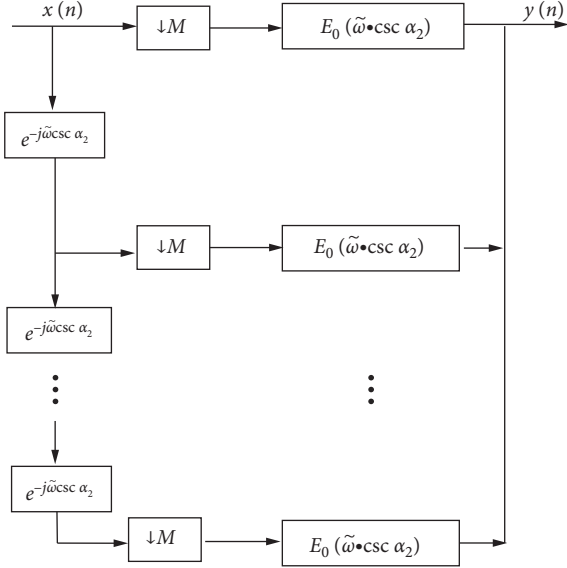


FIGURE 10: Moving the polyphase components.

where $m_\alpha = \int_{-\infty}^{\infty} u |X_\alpha(u)|^2 du / \int_{-\infty}^{\infty} |X_\alpha(u)|^2 du$ is the normalized first-order origin moment of $X_\alpha(u)$ and $\omega_\alpha = \int_{-\infty}^{\infty} u^2 |X_\alpha(u)|^2 du / \int_{-\infty}^{\infty} |X_\alpha(u)|^2 du$ is the normalized second-order origin moment of $X_\alpha(u)$. The NSOCM $p_\alpha, p_{\alpha+1}$ represent the time width and frequency width of $X_\alpha(u)$, respectively. Hence, equation (33) becomes

$$\alpha_{\text{opt}} = \arg \min_{\alpha} \{p_\alpha \cdot p_{\alpha+1}\}, \quad 0 \leq \alpha < \frac{\pi}{2}. \quad (35)$$

The NSOCM product is given by

$$p_\alpha \cdot p_{\alpha+1} = p_0 \cdot p_1 + \frac{1}{4} \left[(p_0 - p_1)^2 - 4\mu_0^2 \right] \sin^2(\alpha\pi) + \frac{1}{2} \mu_0 (p_0 - p_1) \sin(2\alpha\pi), \quad (36)$$

where $\mu_0 = (\omega_0 + \omega_1)/2 + m_0 m_1 - \omega_{0.5}$ is the mixed second-order moment. Setting the first derivative of $p_\alpha \cdot p_{\alpha+1}$ with respect to the order α equal to zero, we obtain

$$\tan(2\alpha_e\pi) = \frac{[4\mu_0(p_0 - p_1)]}{[4\mu_0^2 - (p_0 - p_1)^2]}. \quad (37)$$

For this case where α is equal to the extreme point α_e , the product $p_\alpha \cdot p_{\alpha+1}$ reaches the extremum values. This result demonstrates that when α satisfies equation (38) as follows, the product $p_\alpha \cdot p_{\alpha+1}$ reaches its minimum.

$$\begin{cases} 0 \leq \alpha \leq \frac{\pi}{2}, \\ \alpha = \frac{1}{4} \arctan\left(\frac{4\mu_0(p_0 - p_1)}{4\mu_0^2 - (p_0 - p_1)^2}\right) + \frac{n\pi}{4}, \\ \frac{\mu_0(p_0 - p_1)}{\sin(2\alpha\pi)} > 0. \end{cases} \quad (38)$$

Based on the theoretical analysis above, the calculation process of the optimal transform order can be summarized into the specific procedures as follows:

- (1) Take the 0.5th- and 1st-order DTSFrFT of signal $x[n]$ to obtain $X_{0.5}, X_1$
- (2) Calculate the normalized first-order origin moments m_0 and m_1 , the normalized second-order origin moments $\omega_0, \omega_{0.5}$, and ω_1 , the mixed second-order moment μ_0 , and NSOCM p_0 and p_1 in accordance with the definition
- (3) Obtain the optimal order α_{opt} of α by using (38) in the range of $[0, \pi/2]$.

And the flowchart is shown in Figure 11.

4. Discussion

4.1. Special Cases for Deterministic Signals. The above system as shown in Figure 4 is suitable for the chirp-stationary random signals which have random characters. We have analyzed the output of the system and obtained the conclusion that the proposed system can sense the fractional power spectrum of the chirp-stationary random signals effectively. When the input signals of the system are deterministic signals which have compact support in the FrFD, the cross-correlation analysis is equivalent to the convolution theorem in the sense of FrFT. And special forms of the outputs occur.

When $x(n)$ is a deterministic signal, suppose that $\bar{u}_k(MNn)$ is the output of filter bank $\bar{H}_{k,\alpha_2}(\omega)$, $k = 0, \dots, M-1$, $\bar{v}_l(MNn)$ is the output of filter bank $\bar{G}_{l,\alpha_2}(\omega)$, $l = 0, \dots, N-1$, and the two filter banks have a common input $x(n)$. Then, the product of the multiband filters $\bar{H}_{k,\alpha_2}(\omega)$ and $\bar{G}_{l,\alpha_2}(\omega)$ is

$$\begin{aligned} \bar{F}_{kl,\alpha_2}(\omega) &= \bar{H}_{k,\alpha_2}(\omega) \bar{G}_{l,\alpha_2}(\omega) \\ &= \bar{H}_{\alpha_2} \left(e^{j\tilde{\omega}N \text{csc} \alpha_2} U_M^k \right) \bar{G}_{\alpha_2} \left(e^{j\tilde{\omega}N \text{csc} \alpha_2} U_N^l \right), \end{aligned} \quad (39)$$

$$\begin{aligned} \bar{u}_k(MNn) &= \left[x(n) e^{j1/2n^2T^2 \cot \alpha_1} * h_0(n) \right] \\ &= \left\{ \left[x(n) e^{j1/2n^2T^2 \cot \alpha_1} * h_0(n) \right] e^{-j1/2n^2T^2 \cot \alpha_2} \right\} \\ &\quad \cdot e^{j1/2n^2T^2 \cot \alpha_2}. \end{aligned} \quad (40)$$

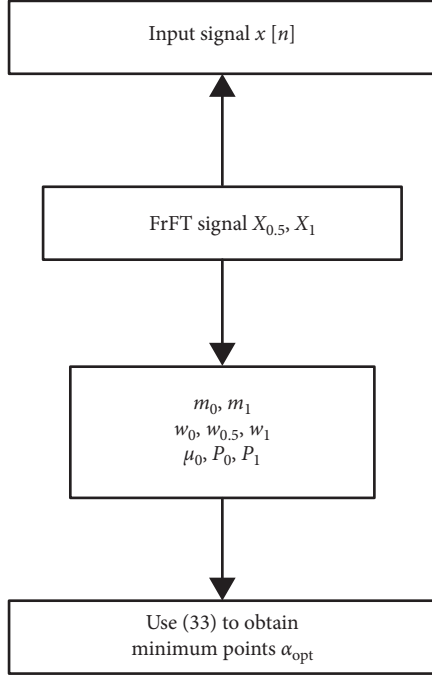


FIGURE 11: Flowchart of the optimal transformation order calculation.

According to the fractional convolution theorem in Section 2.4, the spectrum of $[x(n)e^{j1/2n^2T^2 \cot \alpha} * h_0(n)]e^{-j1/2n^2T^2 \cot \alpha_2}$ in FrFD is

$$\sqrt{2\pi} \tilde{X}_{\alpha_2}(\omega) \bar{H}_{\alpha_2}(\omega), \quad (41)$$

$$\begin{aligned} \bar{v}_1(MNn) &= \left[x(n)e^{j1/2n^2T^2 \cot \alpha_1} * g_0(n) \right] \\ &= \left\{ \left[x(n)e^{j1/2n^2T^2 \cot \alpha_1} * g_0(n) \right] e^{-j1/2n^2T^2 \cot \alpha_2} \right\} \\ &\quad \cdot e^{j1/2n^2T^2 \cot \alpha_2}. \end{aligned} \quad (42)$$

According to the convolution theorem in FrFD, the spectrum of $[x(n)e^{j1/2n^2T^2 \cot \alpha_1} * g_0(n)]e^{-j1/2n^2T^2 \cot \alpha_2}$ in FrFD is

$$\sqrt{2\pi} \tilde{X}_{\alpha_2}(\omega) \bar{G}_{\alpha_2}(\omega). \quad (43)$$

So, the final output of the system is

$$y(n) = \bar{u}_k(MNn) * \bar{v}_1(MNn), \quad (44)$$

where $*$ denotes the traditional convolution operator.

The spectrum of $y(n)$ in FrFD is

$$\begin{aligned} \tilde{Y}(\omega) &= e^{-j\omega^2/2T^2 \cot \alpha_2} \left[\sqrt{2\pi} \tilde{X}_{\alpha_2}(\omega) \bar{H}_{\alpha_2}(\omega) \right] \\ &\quad \left[\sqrt{2\pi} \tilde{X}_{\alpha_2}(\omega) \bar{G}_{\alpha_2}(\omega) \right]. \end{aligned} \quad (45)$$

According to (2), there is

$$\begin{aligned} \bar{Y}(\omega) &= e^{-j\omega^2/2T^2 \cot \alpha_2} \left[\sqrt{2\pi} \tilde{X}_{\alpha_2}(\omega) \bar{H}_{\alpha_2}(\omega) \right] \left[\sqrt{2\pi} \tilde{X}_{\alpha_2}(\omega) \bar{G}_{\alpha_2}(\omega) \right] \\ &= 2\pi e^{j\omega^2/2T^2 \cot \alpha_2} \left[\bar{X}_{\alpha_2}(\omega) \right]^2 \left[\bar{H}_{\alpha_2}(\omega) \bar{G}_{\alpha_2}(\omega) \right], \end{aligned} \quad (46)$$

and since $\bar{Y}_{\alpha_2}(\omega) = e^{-j\omega^2/2T^2 \cot \alpha_2} \tilde{Y}_{\alpha_2}(\omega)$, we have

$$\bar{Y}(\omega) = 2\pi \left[\bar{X}_{\alpha_2}(\omega) \right]^2 \left[\bar{H}_{\alpha_2}(\omega) \bar{G}_{\alpha_2}(\omega) \right], \quad (47)$$

that is, in DTSFrFD, the system output which is shown in Figure 12 is the square of the fractional spectrum of deterministic signal $x(n)$. And this conclusion can be used to estimate the fractional spectrum $\bar{X}_{\alpha_2}(\omega)$.

4.2. Simulation. We demonstrate the simulations for three different cases: resolution performance, the sensing accuracy, and the influence of the order α .

4.2.1. Resolution Performance. In this experiment, we will examine the resolution performance of our proposed method. The traditional DFT coprime filter banks structure [35] and the conventional polyphase filter banks [48] are given for comparison. The original multiband signal is denoted by $z(t)$. And the noisy signal is $z(t) + n(t)$, where $n(t)$ is white Gaussian noise. And $z(t)$ is given by the following:

$$z(t) = \sum_{i=1}^2 z_i(t) \quad (48)$$

$$= \sum_{i=1}^2 E_i \text{rect}\left(\frac{t - \tau_i}{s_i}\right) e^{j\pi K_i t^2} \cos(2\pi f_i t).$$

The choices of the parameters are listed in Table 1.

The optimal orders [34] of $z_1(t)$ and $z_2(t)$ are $\alpha_{z_1} = \arccot(-K_1) = -5.0 \times 10^{-9}$, $\alpha_{z_2} = \arccot(-K_2) = -5.6 \times 10^{-9}$; $z_1(t)$ and $z_2(t)$ have the best energy concentration at orders α_{z_1} and α_{z_2} , respectively. For the system shown in Figure 4, we set $M = 11$ and $N = 7$. And the sampling frequency is $N = 7$. The individual filter banks could only have resolved separations $|2\pi \sin \alpha_2 / 11| = |0.5712 \sin \alpha_2|$ and $|2\pi \sin \alpha_2 / N| = |0.8976 \sin \alpha_2|$, respectively. However, the coprime DFrFT filter banks could have resolved separations $|2\pi \sin \alpha_2 / (MN)| = |0.0816 \sin \alpha_2|$, which is more effective than the individual filter banks. The output of the original system [35] is shown in Figure 13(a); the fractional spectrum estimation in the $\alpha\pi/2 \approx -9.26 \times 10^{-9}$ FrFD is plotted in Figure 13(b). And it can be seen from Figure 13 that the outputs of the original system are overlapped in FD while the outputs of the proposed system are separated from each other in DTSFrFD with order $\alpha\pi/2 \approx -9.26 \times 10^{-9}$.

Figure 14 shows the resolution for different numbers of channels. In Figure 14, the number of channels (i.e., $M + N$) varies from 10 to 50 with a step of 10. And appropriate M and N which are coprime are selected corresponding to every number of channels to reach the maximum resolution. For example, when the number of channels is 10, there are three coprime pairs: (1, 9), (3, 7), and (5, 5), and we set $M = 5$ and $N = 5$ to get the maximum resolution. The maximum resolution of the proposed system is $2\pi \sin \alpha_2 / (MN)$ while the coprime DFT filter banks is $2\pi / (MN)$. It is observed that in Figure 14, the proposed system has the best performance

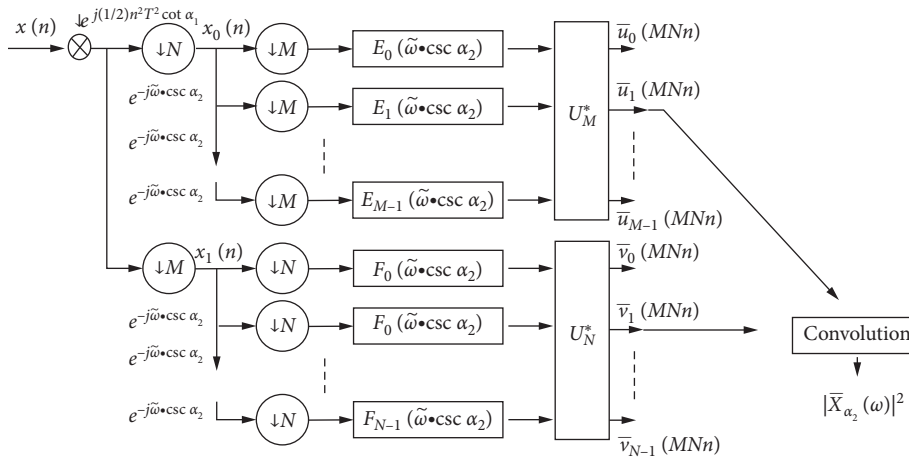


FIGURE 12: Polyphase representation of the coprime DFrFT filter banks for deterministic signals.

TABLE 1: Choices of parameters for deterministic signals.

		Meaning
f_s	1 GHz	Sampling frequency
K_1	0.2×10^9	The signal modulation rate of $z_1(t)$
K_2	0.18×10^9	The signal modulation rate of $z_2(t)$
s_1	$10 \mu\text{s}$	Signal duration of $z_1(t)$
s_2	$10 \mu\text{s}$	Signal duration of $z_2(t)$
f_1	90 MHz	Frequency carrier of $z_1(t)$
f_2	105 MHz	Frequency carrier of $z_2(t)$

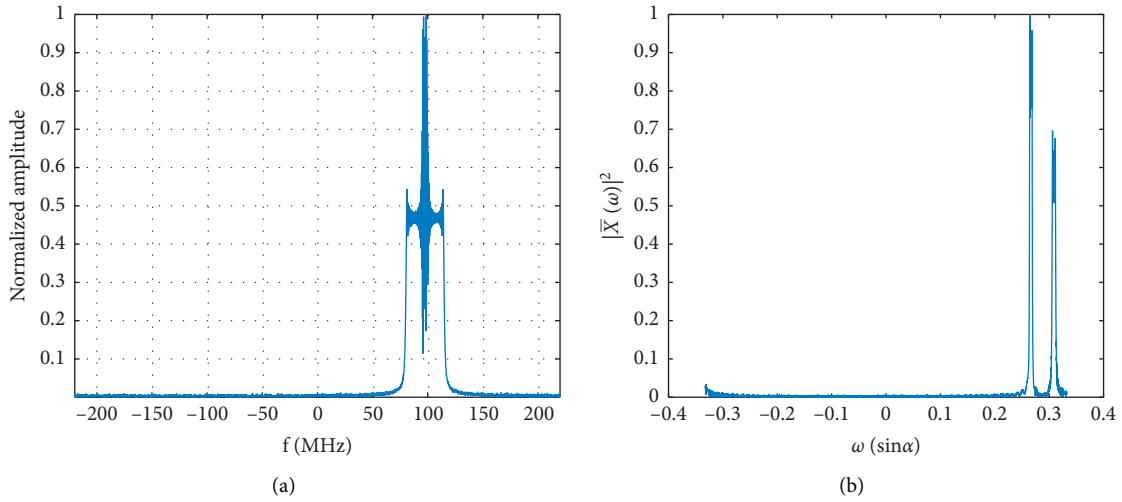


FIGURE 13: Output of the coprime DFT filter banks and the coprime DSFrFT filter banks.

because the parameter $\sin \alpha$ is introduced into the system by DTSSFrFT as analyzed in Section 3.3. Figure 14 also shows that our method has better performance when the number of channels increases. Thus, in practical applications, the proposed system is more cost-effective than the traditional coprime DFT filter banks.

4.2.2. Spectrum Sensing Accuracy. In the second experiment, we test the spectrum sensing accuracy of our proposed

coprime DFrFT filter banks, compared with traditional coprime DFT filter banks [35], spectrum reconstruction technique [49], and non-undersampling method [50].

To evaluate the sensing accuracy of the proposed system as shown in Figure 4, a chirp-stationary random signal $x(t)$ with the initial uniformly distributed random phase φ is considered. And $x(t)$ is given by the following:

$$x(t) = E \cdot \text{rect}\left(\frac{t-\tau}{s}\right) \exp(j\pi Kt^2 + j2\pi ft + j\varphi), \quad (49)$$

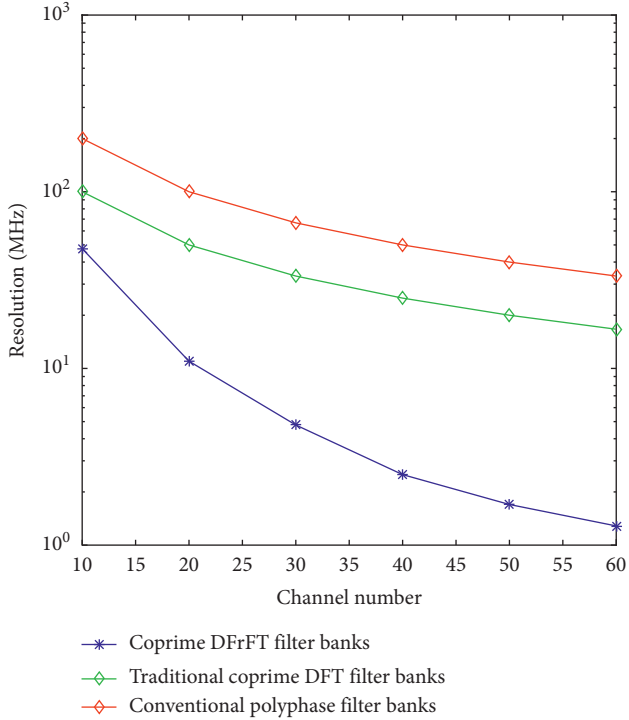


FIGURE 14: Resolution vs. channel number.

where E is the amplitude of the signal which could be fixed. s is the time scale factor which determines the signal duration. K is the signal modulation rate. f is the frequency carrier. $\text{rect}(\cdot)$ is a rectangular time-window denoted by $\text{rect}(t) = 0$, if $|t| > 1/2$; else, $\text{rect}(t) = 1$. The choices of the parameters for $x(t)$ are listed in Table 2.

We specify two coprime integers $M = 11$ and $N = 7$, and based on the definition of α^{th} chirp-stationary signal, we can calculate the fractional order $\alpha_1 = \text{arccot}(-2K\pi) = -8 \times 10^{-10}$ and the optimal transformation order $\alpha_2 = -7 \times 10^{-10}$. The SNR ranges from 0 dB to 20 dB with step size 2 dB. Here, we define the spectrum sensing accuracy as

$$\varepsilon = \sqrt{\frac{1}{N} \sum_{n=1}^N \left[\left(\widehat{f}_n^l - f_n^l \right)^2 + \left(\widehat{f}_n^u - f_n^u \right)^2 \right]}, \quad (50)$$

where \widehat{f}_n^l and \widehat{f}_n^u are the estimated lower boundary and upper boundary in the j^{th} Monte Carlo simulation, respectively. f_n^l and f_n^u are the true lower boundary and upper boundary. Here, 200 Monte Carlo simulations are used.

The original input signal $x(t)$ in the temporal domain is shown in Figure 15(a), and the outputs in the $\alpha_2 = -7 \times 10^{-10}$ FrFD are plotted in Figure 15(b). From the results in Figure 15, the fractional powers spectrum of the α^{th} chirp-stationary signal $x(t)$ can be sensed effectively by the proposed method. And the simulation results are consistent with the analysis in Section 3.

Figure 16 shows the sensing accuracy for different SNRs. In Figure 16, non-undersampling method has the best

TABLE 2: Choices of the parameters for a chirp-stationary random signal.

		Meaning
f_s	1 GHz	Sampling frequency
K	2×10^9	The signal modulation rate of $x(t)$
s	10 μ s	Signal duration of $x(t)$
f	90 MHz	Frequency carrier of $x(t)$

performance because it uses all Nyquist samples in signal processing. However, the results do not preclude the usefulness of the proposed method because the sampling rate of our method is far lower than the Nyquist sampling rate which will greatly reduce the pressure of ADC. Figure 16 also shows that our method has better performance for sensing chirp-stationary random signal than the traditional DFT coprime filter banks. This is because the traditional DFT coprime filter banks is suitable for sensing the power spectrum of wide-sense stationary (WSS) signals, while our proposed system has the ability of sensing the power spectrum of nonstationary signals. The sensing accuracy of the spectrum reconstruction technique improves gradually with the increase in SNR. However, As plotted in Figure 16, our proposed coprime DFrFT filter banks outperform the spectrum reconstruction technique. The explanation for this phenomenon is that cross-interference during reconstruction is so severe that the sensing accuracy is greatly affected by it.

4.2.3. Simulation of Influence of the Order α . According to the analysis in Section 3.7, the α^{th} -order SFrFT can be regarded as the projection on the rotated frequency axis u ; consequently, the spectrum distribution of the signal directly depends on the transform order of the SFrFT. When the transform order α_2 is equal to the optimal transformation order α_{opt} , the energy of signals are concentrated maximally, and the fractional power spectrum is a pulse, which maximizes the sensing accuracy. Correspondingly, an inaccurate order may lead to changes in the spectral width. If the bandwidth of the real spectrum is wider than the bandwidth of the theoretical order, then the real maximum bandwidth will be bigger than the sampling rate. This will result in spectrum aliasing. The spectrum sensing accuracy will rapidly decrease.

In the last experiments, we demonstrate the influence of the order α_2 on the spectrum sensing accuracy. The tested signal is the same as that in Section 4.2.2, and we show the balance between the sensing accuracy and the transform order α_2 in the noise-free and noisy cases. Each simulation has 300 trials to ensure statistically stable results.

As the optimal transformation order of the tested signal is $\alpha_{\text{opt}} = -7 \times 10^{-10}$, we investigate the sensing accuracy under different α_2 where α_2 varies from -0.80×10^{-9} to -0.60×10^{-9} with a step of 0.01×10^{-9} , the SNR is $\{5, 15\}$ dB. It can be seen from Figure 17 that the closer to -0.70×10^{-9} the transform order α_2 is, the smaller the estimation error is. Conversely, the closer to -0.80×10^{-9} or -0.60×10^{-9} , the larger the error is. Furthermore, the sensing

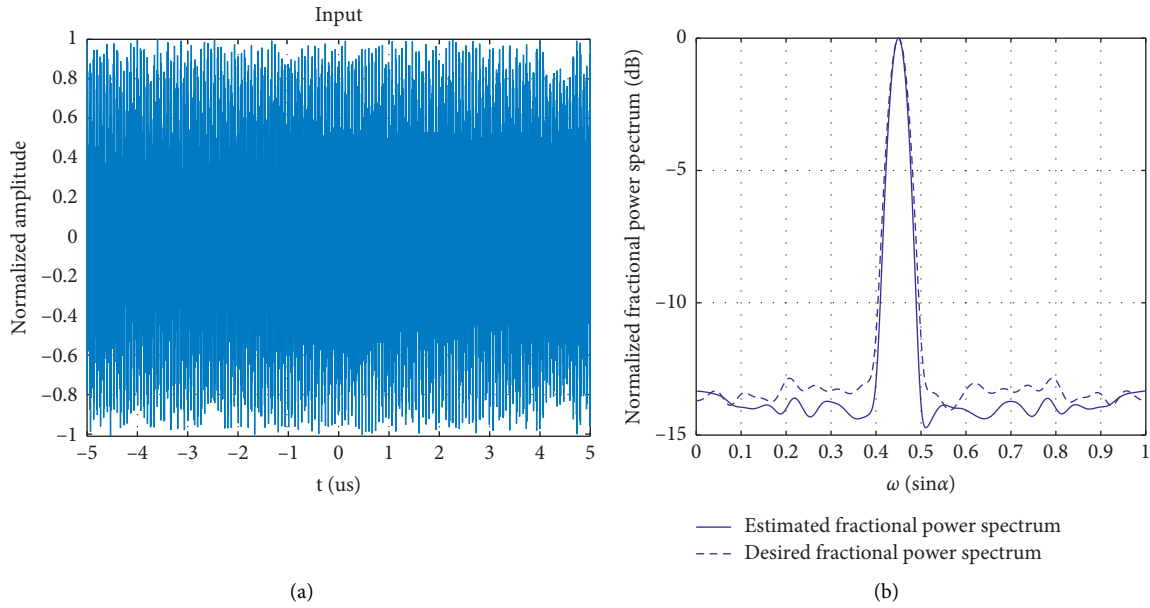


FIGURE 15: Input signal and its fractional power spectrum.

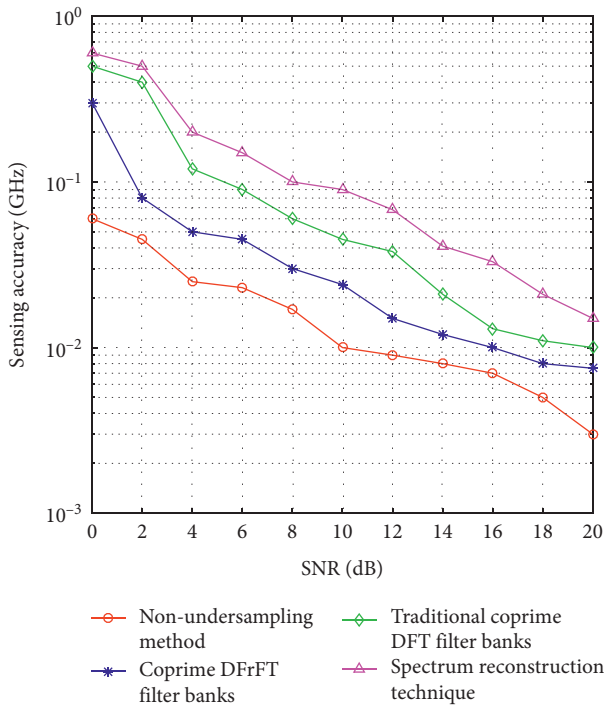


FIGURE 16: Sensing accuracy vs. SNR.

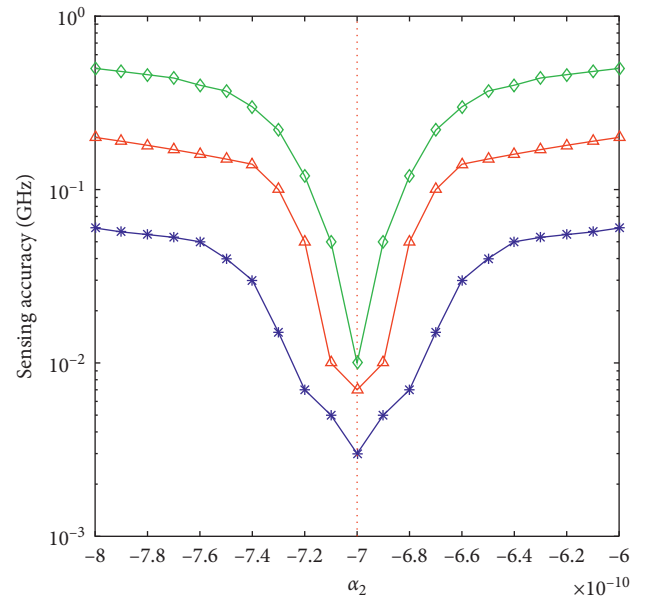


FIGURE 17: The relationship between the sensing accuracy and transform order α_2 in the noisy case and noise-free case.

accuracy in noise-free case is the best because that the signal is not polluted by the noise.

Figure 18 depicts the performance in terms of sensing accuracy with different SNRs and fractional order α_2 for the proposed method. The SNR varies from 0 dB to 20 dB with a step of 2 dB. The fractional order α_2 varies from -0.80×10^{-9} to -0.60×10^{-9} with a step of 0.01×10^{-9} . It is observed that the sensing accuracy has the opposite trend as the SNR.

Furthermore, both Figures 17 and 18 indicate that if the transform order α_2 is close to the optimal order α_{opt} , the sensing accuracy will be improved particularly fast. Therefore, the proposed system is sensitive to the transform order α_2 , especially when the value of α_2 is near α_{opt} . So, how to enhance the robustness of the system is a problem that needs to be further studied.

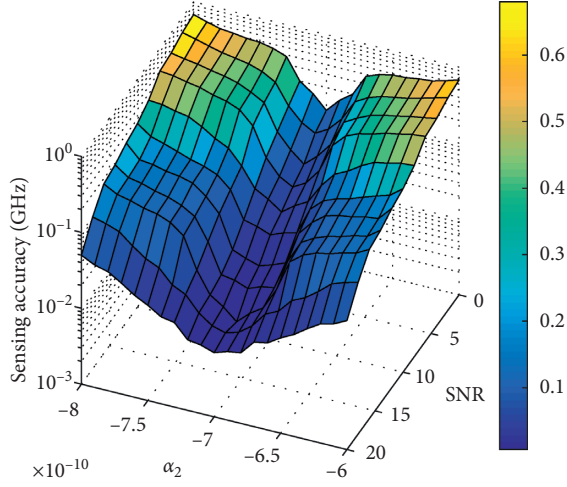


FIGURE 18: Performance of sensing accuracy in 3D space.

5. Conclusion

This paper puts forward coprime DFrFT filter banks for sensing the fractional power spectrum of the nonstationary signals. We gave a deep analysis on the mechanism that the nonstationary signals cannot be effectively sensed by the original coprime DFT filter banks. By means of the relationship between FrFT theory and FT theory, the modified coprime DFrFT filter banks can sense the fractional power spectrum of the nonstationary signals precisely. Furthermore, the proposed coprime DFrFT filter banks obtain a better resolution scaled by $\sin \alpha$ than the original coprime DFT filter banks as well. And the special case for deterministic signals is also discussed based on the convolution theorem in DTSFrFD. Simulation results have shown that our proposed method outperforms traditional coprime DFT filter banks in sensing the fractional power spectrum of nonstationary signals. The further work should address the problem of the robustness of the system to the transform order α_2 .

Nomenclature

FT:	Fourier transform
FD:	Fourier domain
DFT:	Discrete Fourier transform
DFrFT:	Digital fractional Fourier transform
DTFT:	Discrete-time Fourier transform
DTFD:	Discrete-time Fourier domain
FrFT:	Fractional Fourier transform
FrFD:	Fractional Fourier domain
SFrFT:	Simplified fractional Fourier transform
SFrFD:	Simplified fractional Fourier domain
DSFrFT:	Digital simplified fractional Fourier transform
DTFrFT:	Discrete time fractional Fourier transform
DTFrFD:	Discrete time fractional Fourier domain
DTSFrFT:	Discrete-time simplified fractional Fourier transform
DTSFrFD:	Discrete-time simplified fractional Fourier domain

WSS: Wide-sense stationary
LTI: Linear time invariant.

Appendix

Proof of Theorem 2

Theorem 2. Given any integer i in $0 \leq i \leq MN - 1$, there is a unique $\bar{F}_{kl,\alpha}(\omega)$, i.e., a unique (k, l) pair, with passband centered at $2\pi i \sin \alpha / (MN)$.

Proof. The normalized band locations of $\bar{H}_{k,\alpha}(\omega)$ and $\bar{G}_{l,\alpha}(\omega)$ are

$$\frac{2\pi n \sin \alpha}{N} + \frac{2\pi k \sin \alpha}{MN} = (Mn + k) \frac{2\pi \sin \alpha}{MN}, \quad 0 \leq n \leq N - 1, \quad (\text{A.1})$$

$$\frac{2\pi m \sin \alpha}{M} + \frac{2\pi l \sin \alpha}{MN} = (Nm + l) \frac{2\pi \sin \alpha}{MN}, \quad 0 \leq m \leq M - 1, \quad (\text{A.2})$$

and they can be written as

$$Mn + k, \quad 0 \leq n \leq N - 1, 0 \leq k \leq M - 1, \quad (\text{A.3})$$

$$Nm + l, \quad 0 \leq m \leq M - 1, 0 \leq l \leq N - 1. \quad (\text{A.4})$$

Given any integer i in $0 \leq i \leq MN - 1$, there is a unique pair (n, k) (quotient and remainder of i modulo M) such that $i = Mn + k$. Similarly, there is a unique pair (m, l) such that $i = Nm + l$. Thus, the filter $\bar{F}_{kl,\alpha}(\omega)$ has passband centered at $2\pi i \sin \alpha / (MN)$.

Theorem 2 is proved. \square

Proof of Theorem 3

Theorem 3. $\bar{F}_{kl,\alpha}(\omega)$ has precisely one passband, and it has width $2\pi \sin \alpha / (MN)$. That is, there is only one overlapping band among the N bands of $\bar{H}_{k,\alpha}(\omega)$ and M bands of $\bar{G}_{l,\alpha}(\omega)$. This overlapping passband is centered at $2\pi i \sin \alpha / (MN)$ for some integer i in $0 \leq i \leq MN - 1$.

Proof. Assume the contrary. Thus, suppose $F_{kl,\alpha}(\omega)$ has two passbands, centered at $Mn + k = Nm' + l$ and $Mn' + k = Nm' + l$. Thus,

$$\frac{n - n'}{N} = \frac{m - m'}{M}, \quad (\text{B.1})$$

that is,

$$\frac{n - n'}{m - m'} = \frac{N}{M} \quad (\text{B.2})$$

However, since $|m - m'| < M$ and $|n - n'| < N$, this contradicts the coprimality of M and N .

Thus, Theorem 3 is proved. \square

Proof of Theorem 4

Theorem 4. *The relationship between the α^{th} fractional power spectrum of the α^{th} chirp-stationary random sequence $x(n)$ and the conventional power spectrum of the stationary random sequence $\tilde{x}(n) = x(n)e^{jn^2T^2/2\cot\alpha}$ is*

$$\tilde{P}_x(\tilde{\omega} \csc \alpha) = \sqrt{\frac{1}{1 + j \cot \alpha}} P_{xx}^\alpha(\omega), \quad (\text{C.1})$$

in which $\tilde{P}_x(\tilde{\omega} \csc \alpha)$ is the conventional power spectrum of $\tilde{x}(n)$ in discrete-time Fourier domain (DTFD) and $P_{xx}^\alpha(\omega)$ is the α^{th} fractional power spectrum of $x(n)$ in DTSFrFD.

Proof. The autocorrelation of random sequence $\tilde{x}(n)$ is

$$\tilde{R}_{xx}(m) = \tilde{R}_{xx}(n_1, n_2) = R_{xx}(n_2 + m, n_2) e^{j1/2 \cot \alpha T^2 (m^2 + 2n_2 m)}, \quad (\text{C.2})$$

$$\tilde{x}(n) = x(n) e^{jn^2T^2/2\cot\alpha}, \quad (\text{C.3})$$

which is stationary random sequence, so

$$R_{xx}(n_2 + m, n_2) e^{j1/2 \cot \alpha T^2 (m^2 + 2n_2 m)} \quad (\text{C.4})$$

is just a function related to m , and so

$$R_{xx}(n_2 + m, n_2) = e^{-jT^2 \cot \alpha n_2 m} \hat{R}_{xx}^\alpha(m). \quad (\text{C.5})$$

Since

$$\hat{R}_{xx}^\alpha(m) = \lim_{M \rightarrow \infty} \frac{1}{2M+1} \sum_{n_2=-M}^M R_{xx}(n_2 + m, n_2) e^{jn_2 m T^2 \cot \alpha}, \quad (\text{C.6})$$

we have

$$\hat{R}_{xx}^\alpha(m) = \hat{R}_{xx}(m). \quad (\text{C.7})$$

Then, according to the definition of the power spectrum of the stationary discrete random process in DTFD, there is

$$\begin{aligned} \hat{P}_x(u) &= \sqrt{\frac{1}{2\pi}} \sum_{m=-\infty}^{\infty} \hat{R}_{xx}(m) e^{-jumT} \\ &= \sqrt{\frac{1}{2\pi}} \sum_{m=-\infty}^{\infty} \hat{R}_{xx}^\alpha(m) e^{j1/2 m^2 T^2 \cot \alpha} e^{-jumT}. \end{aligned} \quad (\text{C.8})$$

Thus, we can observe from (C.8) that $\tilde{P}_x(u)$ can be seen as a DTSFrFT of $\hat{R}_{xx}^\alpha(m)$. According to the definition of discrete-time signal power spectrum at angle α in FRFD,

$$P_{xx}^\alpha(u) = A_{-\alpha} F^\alpha[\hat{R}_{xx}^\alpha(m)](u) e^{-ju^2/2\cot\alpha}. \quad (\text{C.9})$$

It can be seen that $P_{xx}^\alpha(u)$ is the DTSFrFT of $\hat{R}_{xx}^\alpha(m)$. Combining equations (C.8) and (C.9), for chirp-stationary random sequences $x(n)$ at angle α ,

$$\tilde{P}_x(u \csc \alpha) = \sqrt{\frac{1}{1 + j \cot \alpha}} P_{xx}^\alpha(u), \quad (\text{C.10})$$

where $\tilde{P}_x(u \csc \alpha)$ is the power spectrum of $\tilde{x}(n)$ and $P_{xx}^\alpha(u)$ is the power spectrum of $x(n)$ in DTSFrFD at angle α . Substituting $u = \tilde{\omega}/T$ into equation (C.10),

$$\tilde{P}_x(\tilde{\omega} \csc \alpha) = \sqrt{\frac{1}{1 + j \cot \alpha}} P_{xx}^\alpha(\omega). \quad (\text{C.11})$$

Thus, Theorem 4 is proved. \square

Data Availability

No data were used to support this study.

Conflicts of Interest

The authors declare that they have no conflicts of interest regarding the publication of this paper.

Acknowledgments

This study was supported by the National Natural Science Foundation of China (no. 61271354) and Henan Province Science and Technology Key Project (no. 142102210431).

References

- [1] Z. C. Yang, L. I. Xiang, and H. Q. Wang, "An overview of space-time adaptive processing technology based on sparsity of space-time power spectrum," *Acta Electronica Sinica*, vol. 42, no. 6, pp. 1194–1204, 2014.
- [2] P. L. Shui and D. C. Li, "Floating small target detection in sea clutter via normalised doppler power spectrum," *IET Radar Sonar & Navigation*, vol. 10, no. 4, pp. 699–706, 2016.
- [3] G. Xiong, C. Xi, D. Li, and W. Yu, "Cross correlation singularity power spectrum theory and application in radar target detection within sea clutters," *IEEE Transactions on Geoscience and Remote Sensing*, vol. 57, no. 6, pp. 3753–3766, 2019.
- [4] G. Xiong, C. Xi, J. He, and W. Yu, "Radar target detection method based on cross-correlation singularity power spectrum," *IET Radar, Sonar & Navigation*, vol. 13, no. 5, pp. 730–739, 2019.
- [5] D. A. Warde and S. M. Torres, "The autocorrelation spectral density for doppler-weather-radar signal analysis," *IEEE Transactions on Geoscience & Remote Sensing*, vol. 52, no. 1, pp. 508–518, 2013.
- [6] P. H. Y. Lee, J. D. Barter, K. L. Beach et al., "Power spectral lineshapes of microwave radiation backscattered from sea surfaces at small grazing angles," *IEE Proceedings—Radar, Sonar and Navigation*, vol. 142, no. 5, pp. 252–258, 1995.
- [7] M.-H. Ka, A. I. Baskakov, V. A. Terechov, and A. A. Kononov, "Estimation of the sea-surface slope variance based on the power spectrum width of a radar scatterometer," *IEEE Geoscience and Remote Sensing Letters*, vol. 10, no. 3, pp. 593–597, 2013.
- [8] C. M. Hoang, M. Kim, and S. H. Kong, "Automatic recognition of general lpi radar waveform using ssd and supplementary classifier," *IEEE Transactions on Signal Processing*, vol. 67, no. 13, pp. 3516–3530, 2019.
- [9] T. R. Kishore and K. D. Rao, "Automatic intrapulse modulation classification of advanced lpi radar waveforms," *IEEE Transactions on Aerospace & Electronic Systems*, vol. 53, no. 2, pp. 901–914, 2017.

- [10] M. A. Govoni, H. Li, and J. A. Kosinski, "Range-doppler resolution of the linear-fm noise radar waveform," *IEEE Transactions on Aerospace and Electronic Systems*, vol. 49, no. 1, pp. 658–664, 2013.
- [11] S. Liu, S. Tao, Y. D. Zhang, T. Ran, and F. Yuan, "A fast algorithm for multi-component lfm signal analysis exploiting segmented dpt and sdrft," in *Proceedings of the 2015 IEEE Radar Conference*, pp. 1139–1143, Arlington, VA, USA, May 2015.
- [12] M. Daković, T. Thayaparan, and L. Stanković, "Time-frequency-based detection of fast manoeuvring targets," *IET Signal Processing*, vol. 4, no. 3, pp. 287–297, 2010.
- [13] E. G. Baxa, "On implementation of the discrete fourier transform-the stuse algorithm for spectral estimation," *IEEE Transactions on Acoustics Speech & Signal Processing*, vol. 37, no. 11, pp. 1763–1765, 2002.
- [14] P. Welch, "The use of fast fourier transform for the estimation of power spectra: a method based on time averaging over short, modified periodograms," *IEEE Transactions on Audio and Electroacoustics*, vol. 15, no. 2, pp. 70–73, 2003.
- [15] T. Lobos, Z. Leonowicz, J. Rezmer, and P. Schegner, "High-resolution spectrum-estimation methods for signal analysis in power systems," *IEEE Transactions on Instrumentation and Measurement*, vol. 55, no. 1, pp. 219–225, 2006.
- [16] F. Yao and T. C. M. Lee, "Spectral density estimation using sharpened periodograms," *IEEE Transactions on Signal Processing*, vol. 55, no. 9, pp. 4711–4716, 2007.
- [17] Y. Ephraim and W. J. J. Roberts, "On second-order statistics of log-periodogram with correlated components," *IEEE Signal Processing Letters*, vol. 12, no. 9, pp. 625–628, 2005.
- [18] S. M. Kay and S. L. Marple, "Spectrum analysis—a modern perspective," *Proceedings of the IEEE*, vol. 69, no. 11, pp. 1380–1419, 1981.
- [19] G. C. Carter and A. H. Nuttall, "Analysis of a generalised framework for spectral estimation. part 1: the technique and its mean value," *IEE Proceedings F Communications, Radar and Signal Processing*, vol. 130, no. 3, p. 239, 1983.
- [20] S. Liu, T. Shan, R. Tao et al., "Sparse discrete fractional fourier transform and its applications," *IEEE Transactions on Signal Processing*, vol. 62, no. 24, pp. 6582–6595, 2014.
- [21] L. B. Almeida, "The fractional fourier transform and time-frequency representations," *IEEE Transactions on Signal Processing*, vol. 42, no. 11, pp. 3084–3091, 1994.
- [22] R. Torres and E. Torres, "Fractional fourier analysis of random signals and the notion of α -Stationarity of the wigner-ville distribution," *IEEE Transactions on Signal Processing*, vol. 61, no. 6, pp. 1555–1560, 2013.
- [23] B. Boashash and S. Ouelha, "Designing high-resolution time-frequency and time-scale distributions for the analysis and classification of non-stationary signals: a tutorial review with a comparison of features performance," *Digital Signal Processing*, vol. 77, pp. 120–152, 2018.
- [24] I. E. Sejdíć and L. Stanković, "Fractional fourier transform as a signal processing tool: an overview of recent developments," *Signal Processing*, vol. 91, no. 6, pp. 1351–1369, 2011.
- [25] H. M. Ozaktas, D. Mendlovic, L. Onural, and B. Barshan, "Convolution, filtering, and multiplexing in fractional fourier domains and their relation to chirp and wavelet transforms," *Journal of the Optical Society of America A*, vol. 11, no. 2, pp. 547–559, 1994.
- [26] X. Y. Meng, R. Tao, and Y. Wang, "The fractional fourier domain analysis of two channel filter banks," *Acta Electronica Sinica*, vol. 36, no. 5, pp. 919–927, 2008.
- [27] X. Y. Meng, R. Tao, and Y. Wang, "Generalized design method of multirate filter banks in the fractional fourier domain," *Acta Electronica Sinica*, vol. 37, no. 9, pp. 2046–2051, 2009.
- [28] X. Meng, R. Tao, and Y. Wang, "Fractional fourier domain analysis of decimation and interpolation," *Science in China Series F: Information Sciences*, vol. 50, no. 4, pp. 521–538, 2007.
- [29] A. Kutay, H. M. Ozaktas, O. Ankan, and L. Onural, "Optimal filtering in fractional fourier domains," *IEEE Transactions on Signal Processing*, vol. 45, no. 5, pp. 1129–1143, 1997.
- [30] A. I. Zayed, "A convolution and product theorem for the fractional fourier transform," *IEEE Signal Processing Letters*, vol. 5, no. 4, pp. 101–103, 1998.
- [31] R. Tao, B. Deng, and Y. Wang, "Research progress of the fractional fourier transform in signal processing," *Science in China Series F*, vol. 49, no. 1, pp. 1–25, 2006.
- [32] Z. Feng and R. Tao, "Fmulti-sampling rate signal processing based on discrete-time fractional fourier transform," *Progress in Natural Science*, vol. 18, no. 1, pp. 93–101, 2008.
- [33] R. Tao, B.-Z. Li, and Y. Wang, "Spectral analysis and reconstruction for periodic nonuniformly sampled signals in fractional fourier domain," *IEEE Transactions on Signal Processing*, vol. 55, no. 7, pp. 3541–3547, 2007.
- [34] T. Ran, Z. Feng, and W. Yue, "Fractional power spectrum," *IEEE Transactions on Signal Processing*, vol. 56, no. 9, pp. 4199–4206, 2008.
- [35] P. P. Vaidyanathan and P. Pal, "Sparse sensing with co-prime samplers and arrays," *IEEE Transactions on Signal Processing*, vol. 59, no. 2, pp. 573–586, 2011.
- [36] S. Liu, Y. Ma, and T. Shan, "Segmented discrete polynomial-phase transform with coprime sampling," *The Journal of Engineering*, vol. 2019, no. 19, pp. 5619–5621, 2019.
- [37] A. Shaker and E. Hüllermeier, "Recovery analysis for adaptive learning from non-stationary data streams: experimental design and case study," *Neurocomputing*, vol. 150, pp. 250–264, 2015.
- [38] C. Wang, J. Wang, and T. Zhang, "Operational modal analysis for slow linear time-varying structures based on moving window second order blind identification," *Signal Processing*, vol. 133, pp. 169–186, 2017.
- [39] B. Boashash, A. Aïssa-El-Bey, and A. Aïssa-El-Bey, "Robust multisensor time-frequency signal processing: a tutorial review with illustrations of performance enhancement in selected application areas," *Digital Signal Processing*, vol. 77, pp. 153–186, 2018.
- [40] C. Cheng, A. Sa-ngasoongsong, O. Beyca et al., "Time series forecasting for nonlinear and non-stationary processes: a review and comparative study," *IIE Transactions*, vol. 47, no. 10, pp. 1053–1071, 2015.
- [41] X. Huang, Y. Han, Z. Yan, H. Xian, and W. Lu, "Resolution doubled co-prime spectral analyzers for removing spurious peaks," *IEEE Transactions on Signal Processing*, vol. 64, no. 10, pp. 2489–2498, 2016.
- [42] J. W. Xiangdong Huang and S. H. A. N. Yuxuan, "High-performance co-prime spectral analysis method based on parallelled all-phase point-pass filtering," *Journal of Electronics & Information Technology*, vol. 42, no. 3, pp. 613–620, 2020.
- [43] P. P. Vaidyanathan and P. Pal, "Theory of sparse coprime sensing in multiple dimensions," *IEEE Transactions on Signal Processing*, vol. 59, no. 8, pp. 3592–3608, 2011.
- [44] Q. Wu and Q. Liang, "Coprime sampling for nonstationary signal in radar signal processing," *Eurasip Journal on Wireless Communications and Networking*, vol. 58, pp. 1–11, 2013.

- [45] S.-C. Pei and J.-J. Ding, "Simplified fractional fourier transforms," *Journal of the Optical Society of America A*, vol. 17, no. 12, pp. 2355–2367, 2000.
- [46] P. P. Vaidyanathan, "Multirate digital filters, filter banks, polyphase networks, and applications: a tutorial," *Proceedings of the IEEE*, vol. 78, no. 1, pp. 56–93, 2002.
- [47] W. Yuqing and P. Zhenming, "The optimal fractional s transform of seismic signal based on the normalized second-order central moment," *Journal of Applied Geophysics*, vol. 129, pp. 8–16, 2016.
- [48] G. Lopez-Risueno, J. Grajal, and A. Sanz-Osorio, "Digital channelized receiver based on time-frequency analysis for signal interception," *IEEE Transactions on Aerospace and Electronic Systems*, vol. 41, no. 3, pp. 879–898, 2005.
- [49] C.-P. Yen, Y. Tsai, and X. Wang, "Wideband spectrum sensing based on sub-nyquist sampling," *IEEE Transactions on Signal Processing*, vol. 61, no. 12, pp. 3028–3040, 2013.
- [50] S. Khorshidi, M. Karimi, and A. R. Nematollahi, "New autoregressive (ar) order selection criteria based on the prediction error estimation," *Signal Processing*, vol. 91, no. 10, pp. 2359–2370, 2011.